Aromaticity controls the excited-state properties of host-guest complexes of nanohoops

G. George[a], O. A. Stasyuk[a], A. A. Voityuk*[a], A. J. Stasyuk*[a,b] and M. Solà*[a]

a. Institut de Química Computacional i Catàlisi and Departament de Química, Universitat de Girona, C/ Maria Aurèlia Capmany 69, 17003 Girona, Catalonia, Spain

b. Faculty of Chemistry, University of Warsaw, Pasteura 1, 02-093 Warsaw, Poland

Abstract

π-Conjugated organic molecules have exciting applications, as materials for batteries, solar cells, light emitting diodes, etc. Among these systems, antiaromatic compounds are of particular interest because of their smaller HOMO–LUMO energy gap compared to aromatic compounds. A small HOMO-LUMO gap is expected to facilitate charge transfer in the systems. Here we report the ground and excited-state properties of two model nanohoops that are nitrogen-doped analogs of recently synthesized [4]cyclodibenzopentalenes – tetramers of benzene-fused aromatic 1,4-dihydropyrrolo[3,2-b]pyrrole (**[4]DHPP**) and antiaromatic pyrrolo[3,2-b]pyrrole (**[4]PP**). Their complexes with $\mathbf{C_{60}}$ fullerene show different behavior upon photoexcitation, depending on the degree of aromaticity. **[4]DHPP** acts as an electron donor, whereas **[4]PP** is a stronger electron-acceptor than $\mathbf{C_{60}}$. Ultrafast charge separation in combination with slow charge recombination we found for **[4]PP⊃$\mathbf{C_{60}}$** indicate a long lifetime of the charge transfer state.

Introduction

The unusual topology of molecular systems is of considerable interest to the scientific community due to their unique chemical and electronic properties. [1, 2] Extended and curved π-conjugated architectures attract attention in view of optoelectronic applications, [3, 4] host-guest chemistry, [5-8] and discovery of new materials. [9, 10] Cycloparaphenylenes (CPPs) – radially π-conjugated nanohoops composed of *para*-linked phenylene rings are one of the most extensively studied class of curved nanostructures. A significant advance in organic chemistry allows precise control of the number of phenylene units in the target nanohoops. [11-13] It has been discovered that CPPs exhibit intriguing size-dependent optical properties. [14] In particular, their light absorption is almost invariant with the nanohoops size, while emission shows a significant red shift as the size decreases. [15] Changing the size on nanohoops is not the only way to modulate their photophysical properties. The introduction of various π-conjugated units into CPPs that act either as electron donor or electron acceptor also provides a powerful tool. [10]

Despite the variety of reported nanohoops containing only phenylene units or other polycyclic donor-acceptor units, they all contain only aromatic fragments. [10] On the other hand, antiaromatic systems seem to be extremely promising as modulators of the nanohoops properties. Antiaromatic molecules have significantly different properties compared to their aromatic counterparts, including a narrow HOMO-LUMO gap and low-lying triplet states.[16-21] In 2020, Esser and co-workers synthesized [12]cycloparaphenylenes containing two antiaromatic dibenzo[*a*,*e*]pentalene (DBP) units. [22] Later, [n]cyclodibenzopentalenes (CDBPs) (with n = 3 and 4), the nanohoops containing exclusively DBP units, were synthesized. [23] The size and cylindrical shape of [4]CDBP allow for efficient placement of C_{60} and C_{70}

fullerenes. The binding constant for [4]CDBP⊃C_{60} in toluene was found to be $(1.35 \pm 0.03)\cdot 10^5$ M^{-1}. Several others nanohoops containing antiaromatic pentalene units have recently been reported. [24, 25]

It is known that the introduction of heteroatoms into a carbon π-conjugated system can dramatically affect its properties. [26, 27] Doping with nitrogen or boron atoms influences the semiconducting and luminescent properties of organic molecules due to changes in the band structure. [28] Doping antiaromatic hydrocarbons with nitrogen leads to an increase in their electron-withdrawing ability. [29, 30]

In this work, we report a theoretical study of aromaticity, electronic and photoinduced electron transfer (PET) properties of the complexes based on **C_{60}** fullerene with nanohoops built from benzene-fused antiaromatic pyrrolo[3,2-b]pyrrole (**PP**) and its aromatic analog 1,4-dihydropyrrolo[3,2-b]pyrrole (**DHPP**). The structural units have already been synthesized and characterized,[31,32] whereas the nanohoops were modeled based on the similarity to [4]CDBP⊃C_{60}. Our aim is to investigate how the (anti)aromaticity of the nanohoop fragments influences their interaction with C_{60} and related charge transfer processes. We show that the excited-state properties of the host-guest complexes are highly sensitive to π-electron delocalization in the nanohoops.

Results and Discussion

Ground state properties

Geometries of [4]cyclodibenzopyrrolopyrrole **[4]PP** and [4]cyclodibenzodihydropyrrolopyrrole **[4]DHPP**, as well as their inclusion complexes with fullerene **[4]PP⊃C_{60}** and **[4]DHPP⊃C_{60}** (Figure 1) were optimized using BLYP-D3(BJ)/def2-SVP functional. [33-36] The formation energies of the complexes were computed with the BLYP/def2-TZVP//BLYP/def2-SVP scheme. The BLYP-D3(BJ) functional was chosen as the DFT functional with the best accuracy-to-cost ratio for non-covalent interactions.[37,38] The quantitative assessment of aromaticity/antiaromaticity as well as the excited-state calculations were performed using the range-separated CAM-B3LYP functional[39] (see computational details in SI), as required for accurate prediction of charge transfer rates. This functional shows the best performance for modeling charge transfer processes in fullerene-based complexes with a mean absolute percentage error of 6.3%.[40]

Aromaticity/Antiaromaticity of nanohoops

In the molecules studied, four units were considered (Figure 1). The first two are particular phenyl (Ring A) and pyrrole (Ring B) subunits, while the last two are an entire **DHPP** or **PP** units and their tetramers, **[4]DHPP** or **[4]PP**. Aromaticity/antiaromaticity of these units were analyzed through harmonic oscillator model of aromaticity (HOMA),[41,42] the electron density of delocalized bond (EDDB) function,[43,44] nucleus independent chemical shifts (NICS),[45,46] and anisotropy of induced current density (ACID).[47]

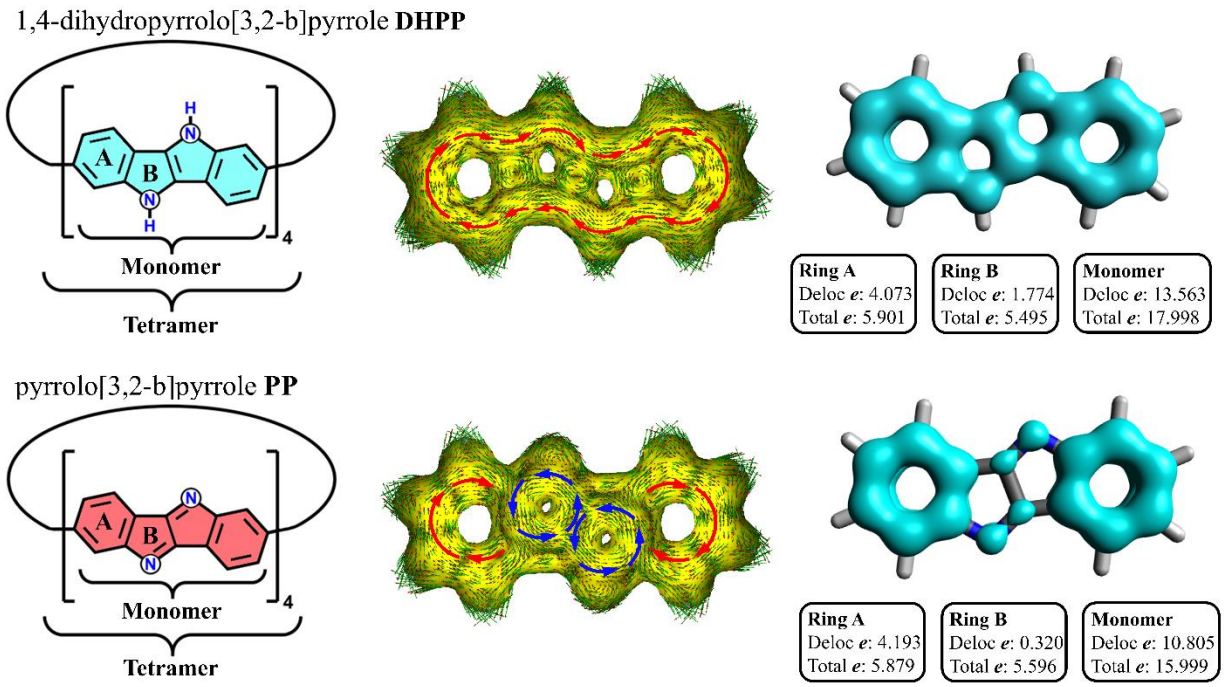

Figure 1. Structure of **DHPP** and **PP** and their ACID and π-EDDB plots.

Initially, the aromaticity of **DHPP** (18 π-electrons) and **PP** (16 π-electrons) monomer molecules was evaluated. Table 1 provides the values of $NICS(1)_{zz}$ and HOMA indices, as well as π-EDDB population. According to the NICS index, defined as a negative value of the absolute magnetic shielding computed at a ring center or at some other point in space, the phenyl rings exhibit substantial aromatic ring currents. $NICS(1)_{zz}$ values, which represent the zz components of the NICS(1) values, for Ring A in **DHPP** and **PP** monomers were found to be -28.9 and -13.0 ppm. In **DHPP**, Ring B also demonstrates a strong aromatic character, even comparable to that found for Ring A. In contrast, in **PP**, the pyrrolic Ring B is characterized by positive $NICS(1)_{zz}$ value of 31.2 ppm that points out to the antiaromatic character of the ring. Note that $NICS(0)_{iso}$ and NICS(1) values provide qualitatively similar results (Table S1, SI). Analysis of the aromaticity based on HOMA and EDDB methods demonstrates an excellent agreement with the NICS results. Indeed, the HOMA and π-EDDB values for Ring A in **DHPP** and **PP** molecules were found fairly similar, while the characteristics of Ring B differs significantly, showing aromatic/antiaromatic nature of five-membered ring in **DHPP/PP.** The global aromaticity of **DHPP** and **PP** molecules (Monomer in Table 1) was calculated using only HOMA and π-EDDB, because single point NICS calculations evaluate only local aromaticity. All π-EDDB values were normalized by a total number of π-electrons involved into delocalization for direct comparison of the results for **DHPP** and **PP** molecules and their tetramers. In **DHPP**, the EDDB analysis revealed the delocalization of electron density over all bonds. When moving to the **PP** system, it becomes clear that the π-electron delocalization is significantly attenuated in Ring B, while it is slightly enhanced in Ring A (Figure 1, Table 1).

Table 1. Aromaticity indices for **DHPP** and **PP** monomers, and corresponding **[4]PP** and **[4]DHPP** tetramers.

Rings	monomer		tetramer	
	DHPP	**PP**	**[4]DHPP**	**[4]PP**

	NICS(1)$_{zz}$			
Ring A	-28.9	-13.0	-21.7	-1.6
Ring B	-23.9	31.2	-17.4	26.5
	HOMA			
Ring A	0.697	0.761	0.650	0.692
Ring B	0.476	-0.489	0.476	-0.514
Monomer	0.661	0.338	0.618	0.299
Tetramer	n/a		0.587	0.360
	π-EDDB$^{Norm[a]}$			
Ring A	0.690	0.713	0.634	0.687
Ring B	0.323	0.057	0.317	0.058
Monomer	0.754	0.675	0.705	0.650
Tetramer	n/a		0.741	0.698

[a] Due to inequivalent ratios of π electrons and atoms in systems, the EDDB values were normalized by the number of π electrons: π-EDDB^{Norm} = π-EDDB/n_π

We observed that the formation of tetramers slightly decreases the aromaticity of the monomer units. This is in line with previous experimental and theoretical studies showing that the π-electron delocalization of aromatic molecules is quite robust and can resist large out-of-plane distortions.[48-50] Formation of the tetrameric macrocycles is associated with a noticeable bending of **DHPP** and **PP** monomers (Figure S1). To evaluate the impact of bending on the aromaticity, the NICS(1)$_{zz}$ and π-EDDB values for monomeric units in macrocyclic and free state geometries were calculated. We found that the bending has relatively small effect on the aromaticity (Table S2, SI).

We used the anisotropy of the induced current density (ACID) method to visualize the ring currents and electron delocalization (Figure 1). In our plots, diatropic currents run clockwise and indicate aromaticity, while paratropic currents run counter-clockwise and indicate antiaromaticity. In the ACID plot for **DHPP**, both benzene rings and inner dihydropyrrolopyrrole unit exhibit diatropic ring currents. Note that partial cancelation of the ring currents observed over the bond between benzene and pyrrole rings as well as between two pyrrole rings in **DHPP** is due to the flow of ring current in opposite directions. In contrast, the ACID plot of **PP** demonstrates the diatropic ring currents in the outer benzene rings and a strong paratropic ring current in the pyrrolo[3,2-b]pyrrole core.

Electronic properties

A relatively large cavity size of **[4]PP** and **[4]DHPP** π-conjugated nanohoops capable of containing **C_{60}** fullerene encouraged us to study their inclusion complexes in detail. First, the orbital energies of the **[4]PP⊃C_{60}** and **[4]DHPP⊃C_{60}** complexes, and their individual fragments were analyzed.

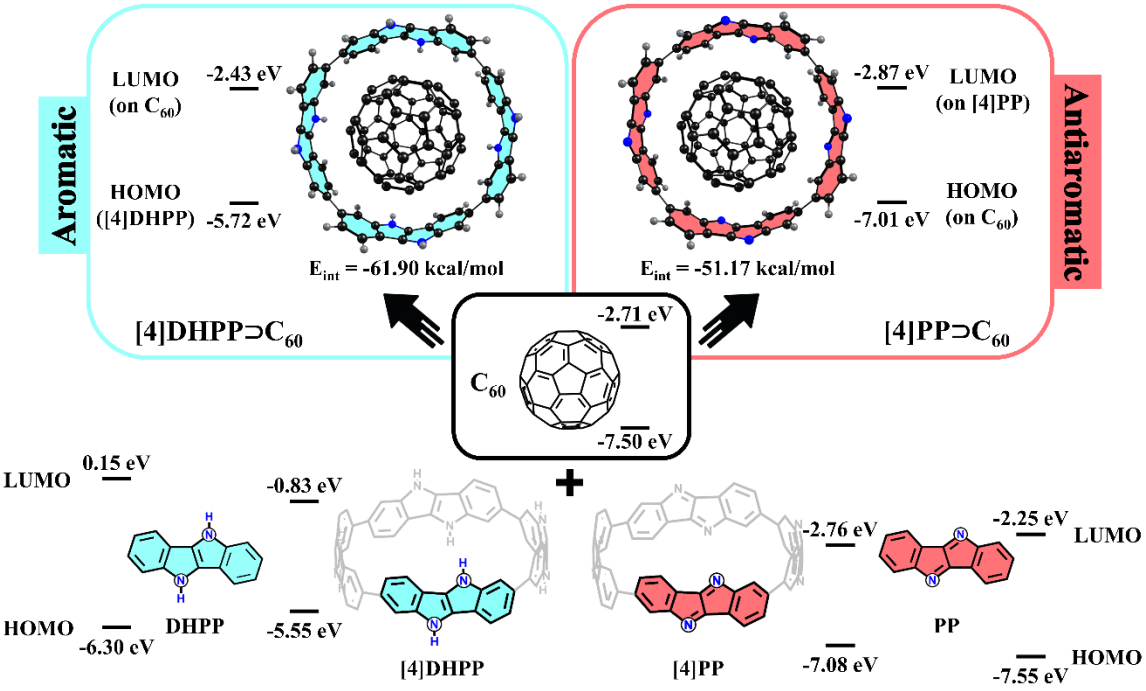

Figure 2. Structures and HOMO/LUMO energies of **[4]DHPP⊃C$_{60}$**, **[4]PP⊃C$_{60}$** complexes and their subunits.

As seen in Figure 2, the HOMO and LUMO energies for **PP, DHPP** and as their cyclic tetramers differ significantly. Antiaromatic compounds usually have much smaller HOMO–LUMO energy gaps than aromatic compounds. Indeed, antiaromatic **PP** has a HOMO-LUMO (HL) gap 1.15 eV smaller than aromatic **DHPP**. When going from aromatic to antiaromatic systems, both HOMO and LUMO undergo a significant stabilization, while LUMO becomes much more stabilized (see Table S3, SI). The observed changes in the orbital energies not only lead to a decrease of the HL gap, but also show that the **PP** system with an antiaromatic fragment is a weaker electron donor and a stronger electron acceptor. The changes in the orbital energies are also visible when going from the **PP** and **DHPP** unit to the corresponding **[4]DHPP** and **[4]PP** nanoohoop. During the formation of tetramers the planar monomeric units undergo a bending deformation (Figure S1, SI). However, this deformation is relatively small and should not cause such noticeable changes. According to the calculations, the difference in the orbital energies caused by bending does not exceed 0.1 eV (Table S3, SI). Thus, the observed changes are most likely of an electronic nature. We compared the orbitals for **PP** and **DHPP** monomers (in equilibrium and geometry of complex) with the orbitals for cyclic tetramers (Figure S2 and S3, SI). The analysis revealed that distribution of HOMO and LUMO in the equilibrium geometry and bended monomers are almost identical, which is in a good agreement with similar values of the orbital energy. In turn, the formation of tetramer is associated with a remarkable orbital redistribution. For **DHPP**-based complex, when going from monomer to tetramer, contribution of nitrogen atomic orbitals to the HOMO decreases excluding nitrogen atoms from the orbital almost completely. As a result, the HOMO energy increases. A similar behavior can be observed when comparing 1,4-diazapentalene and pristine pentalene. Replacing nitrogen atoms with carbons causes an increase in HOMO energy.[29] It should be noted that a wavefunction node, where the wavefunction is zero and changes signs, was found on a single C-C bond connecting **DHPP** units in the tetramer (Figure S3, SI). In the case of LUMO, no large changes in the orbital distribution between the isolated monomer and the monomer in tetramer were found. However, the LUMO on the single C-C bonds between monomers has

a binding character. This leads to better inter-unit communication and increases effective LUMO delocalization.

Important to note that despite the structural similarity, complexes have a different electronic nature. In particular, for **[4]DHPP⊃C$_{60}$**, LUMO is localized on the **C$_{60}$** fragment, while the HOMO is distributed over **[4]DHPP** nanohoop. In contrast, for **[4]PP⊃C$_{60}$**, LUMO is localized on the **[4]PP** nanohoop, which contains antiaromatic fragments, and HOMO is on the **C$_{60}$** fullerene. Taking into account that both complexes can be considered as donor-acceptor systems, we checked the charge separation between the host and guest units in the ground state. However, the population analysis carried out within the most popular schemes (Table S4, SI) did not reveal any noticeable charge transfer between the fragments. The absorption spectra of both complexes was found to be a superposition of absorption spectra of **C$_{60}$** and nanohoops (Figure S4, SI).

The interaction energy (ΔE_{int}) between **C$_{60}$** guest and nanohoop host units was calculated to estimate the stability of the complexes. For **[4]DHPP⊃C$_{60}$** and **[4]PP⊃C$_{60}$** complexes, ΔE_{int} was found to be -61.9 and -51.2 kcal/mol, correspondingly. These values are comparable with the ΔE_{int} values of other inclusion complexes of fullerene, such as **[10]CPP⊃C$_{60}$** (-59.1 kcalmol) and **[4]CDBP⊃C$_{60}$** (-56.8 kcal/mol). In addition, we performed the Morokuma-like energy decomposition analysis (EDA) [51,52] implemented in the ADF program.[53] The EDA decomposes the interaction energy into four components: electrostatic (ΔE_{elstat}), Pauli repulsion (ΔE_{Pauli}), orbital interactions (ΔE_{oi}), and dispersion correction (ΔE_{disp}), and allows one to estimate the role of the specific interactions. The EDA results are shown in Table 2.

Table 2. EDA results for **[4]DHPP⊃C$_{60}$** and **[4]PP⊃C$_{60}$** complexes.[a]

Complex	Energy terms, kcal/mol				
	ΔE_{Pauli}	ΔE_{elstat}	ΔE_{oi}	ΔE_{disp}	ΔE_{int}
[4]DHPP⊃C$_{60}$	156.41	-70.88 (32.5%)	-32.34 (14.8%)	-115.09 (52.7%)	-61.90
[4]PP⊃C$_{60}$	168.95	-72.80 (33.1%)	-31.59 (14.4%)	-115.72 (52.6%)	-51.17

[a] The percentage contributions to the sum of attraction energies ($\Delta E_{elstat} + \Delta E_{oi} + \Delta E_{disp}$) are given in parentheses.

Among the attractive terms ($\Delta E_{elstat} + \Delta E_{oi} + \Delta E_{disp}$), the dispersion dominates with a contribution of 53% for both complexes. The second largest term is the electrostatic attraction with similar contribution of about 33%. The orbital interactions provide 14-15% of the total stabilization interactions. As seen, despite the different electronic structure, the complexes demonstrate a very similar nature of non-covalent interactions. The destabilizing term (Pauli repulsion) for **[4]PP⊃C$_{60}$** is slightly larger than for **[4]DHPP⊃C$_{60}$** (168.95 vs. 156.41 kcal/mol) due to smaller size of the **[4]PP** nanohoop. In free state, the effective radii (mean distance from center to each atom) for **[4]DHPP** and **[4]PP** nanohoops are 6.502 and 6.436 Å, respectively. The formation of the complexes slightly affects them. The radius of **[4]DHPP** increases from 6.502 to 6.517 Å, while the radius of **[4]PP** increases from 6.436 to 6.482 Å (Figures S5, SI). Deformation energy upon complexation is 1.0 kcal/mol for **[4]DHPP** and 2.1 kcal/mol for **[4]PP.** Aromatic and antiaromatic nanohoops demonstrate very similar strain energies, and formation of fullerene inclusion complexes does not significantly change them. The strain energies of **[4]DHPP** in free state and in the complex are 64.1 and 65.1 kcal/mol (for details se SI), while for **[4]PP**-based complexes the strain energy changes from 59.9 to 62.0 kcal/mol (Table S5 in SI).

The topological analysis based on Bader's Atoms in Molecules theory (QTAIM)[54] revealed that in the **[4]DHPP⊃C$_{60}$** and **[4]PP⊃C$_{60}$** complexes there are only π···π interactions between the host and guest units (Table S6). **[4]DHPP⊃C$_{60}$** is characterized by a larger number of bond critical points (BCPs) than **[4]PP⊃C$_{60}$** (22 *vs.* 20). In **[4]PP⊃C$_{60}$**, BCPs were found only between carbon atoms of the fragments. However, in **[4]DHPP⊃C$_{60}$**, BCPs were additionally detected between the nitrogen atoms of the nanohoop and the carbon atoms of the fullerene. QTAIM molecular graphs for the complexes are given in Figure S6, SI. The topology of the host-guest interactions in the complexes was also analyzed using the non-covalent interaction index (NCI).[55] The NCI isosurfaces are evenly distributed between the nanohoops and **C$_{60}$**, and have a similar shape for both complexes, which aromatic and antiaromatic fragments. The reduced density gradient (RDG) plots and NCI isosurfaces are presented in Figures S7 and S8, SI. The energy profiles of the **C$_{60}$** movement through the cavity of both nanohoops show a typical single-potential well with a minimum where the centers of the fullerene and nanohoops coincide (Figure S9), similar to **[10]CPP⊃C$_{60}$**.[56,57] This is consistent with the large NCI isosurface in this region and confirms size complementarity between host and guest units.

Singlet excited states

The different electronic structure of the **[4]DHPP⊃C$_{60}$** and **[4]PP⊃C$_{60}$** complexes in the ground state suggests that their excited-state properties should also be different. To study PET, we applied the computational protocol developed in our previous works, which showed good agreement with experimental observations of charge-separated states in fullerene-based complexes.[8,58] The complexes were divided into 2 fragments: guest **C$_{60}$** and host nanohoop. The electron density distribution was analyzed for the 80 lowest-lying singlet excited states. Three types of the excited states were identified: (1) locally excited (LE) states, in which the exciton is mostly localized either on the guest (LE^{Guest}) or on the host molecule (LE^{Host}) and charge transfer is less than 0.1 ***e*** (CT < 0.1 ***e***); (2) charge transfer (CT) states showing a significant charge separation (CT > 0.8 **e**); and (3) mixed states, where both LE and CT states contribute substantially (0.1 ***e*** < CT < 0.8 ***e***).

In the gas phase, the vertical singlet excitation energies of **[4]DHPP⊃C$_{60}$** range from 1.85 to 4.10 eV. The lowest excited state (at 1.85 eV) was identified as a CT state, where electron density is transferred from **[4]DHPP** to **C$_{60}$** (Table 3). This state can be described as a purely HOMO-LUMO transition with 0.97 ***e*** transferred. The LE^{Guest} state is located at 2.39 eV and corresponds to HOMO-4 to LUMO transition. The LE^{Host} state lies 0.44 eV higher than the LE^{Guest} and corresponds to HOMO to LUMO+6 transition. No other types of CT or LE states were found.

Table 3. Excitation energies (E_x, eV), main singly excited configuration (HOMO(H)–LUMO(L)) and its weight (W), oscillator strength (f), extent of charge transfer (CT, e) or localization of exciton (X) computed for **[4]DHPP⊃C$_{60}$** and **[4]PP⊃C$_{60}$** complexes in the gas-phase (VAC) and dichloromethane (DCM).

	Complex			
	[4]DHPP⊃C$_{60}$		**[4]PP⊃C$_{60}$**	
	VAC	DCM	VAC	DCM
	LE^{Guest} (**C$_{60}$**)			
E	2.389	2.397	2.397	2.405
Transition (W)	H-4 – L (0.58)	H-4 – L (0.57)	H – L+4 (0.86)	H – L+4 (0.44)

f	<0.001	<0.001	<0.001	<0.001
X	0.905	0.915	0.912	0.896
	LE^{Host} (nanohoop)			
E	2.826	2.824	2.145	2.033
Transition (W)	H – L+6 (0.49)	H – L+4	H-1 – L (0.31)	H-1 – L (0.30)
f	0.002	0.033	0.012	0.016
X	0.901	0.902	0.950	0.953
	CT1 (nanohoop → **C_{60}**)			
E	1.846	1.824	3.245	3.117
Transition (W)	H – L (0.97)	H – L (0.97)	H-1 – L+3 (0.41)	H-1 – L+3 (0.33)
f	0.001	0.002	<0.001	<0.001
CT	0.971	0.970	0.917	0.912
	CT2 (**C_{60}** → nanohoop)			
E	n/a[a]	n/a[a]	2.471	1.790
Transition (W)			H – L (0.42)	H – L (0.33)
f			0.004	0.005
CT			0.909	0.905

[a] States of interest are not found within 80 lowest excited states. All the attempts to detect this type of CT state within lowest 120 excited states have not been successful.

The behavior of the **[4]PP⊃C_{60}** complex in the excited state differs significantly from its aromatic analog. In contrast to **[4]DHPP⊃C_{60}**, the lowest excited state at 2.15 eV is the LE^{Host}. Note that the significant stabilization of HOMO and LUMO upon transition from aromatic to antiaromatic system led to the stabilization of the LE^{Host}. In particular, the LE^{Host} in **[4]PP⊃C_{60}** lies 0.68 eV lower than that of **[4]DHPP⊃C_{60}**. The energy of the LE^{Guest} in both systems is almost identical and does not depend on the electronic nature of the host. In the **[4]PP** nanohoop with antiaromatic fragments, the HOMO and LUMO orbitals are lower in energy than HOMO and LUMO of **C_{60}**. Thus, it can be assumed that **[4]PP** would exhibit stronger electron-accepting properties than **C_{60}**. Indeed, analysis of the excited states showed that the electron transfer from the fullerene **C_{60}** to the **[4]PP** nanohoop (CT2) has a much lower energy than the reverse **[4]PP**-to-**C_{60}** transition (CT1). The CT2 is located at 2.47 eV, while the energy of CT1 is 3.25 eV. The natural transition orbitals (NTOs) representing the LE and CT states for both complexes are shown in Figures S10-S11, SI. Higher stability of the "unusual" CT2 state, which can be described as **[4]PP^{-}⊃C_{60}^{+}**, compared to the more expected CT1 (**[4]PP^{+}⊃C_{60}^{-}**), can be associated with the different response of **[4]PP** unit towards loss or gain of electron. Global aromaticity descriptors (EDDB and HOMA) of the **[4]PP** nanohoop in neutral, cationic, and anionic forms indicate that withdrawal of electron and generation of **[4]PP^{+}** decreases the aromaticity of the nanohoop (Figure 3).

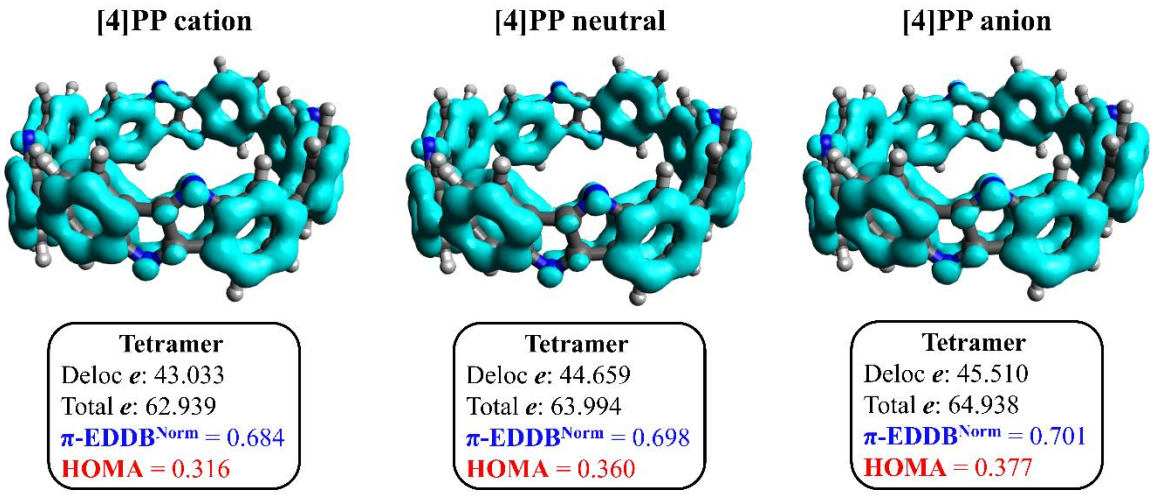

Figure 3. EDDB plots and aromaticity descriptors for **[4]PP** tetramer in its neutral, cationic, and anionic forms.

At the same time, the formation of **[4]PP**$^{-}$ slightly increases the delocalization of π-electrons in the tetramer. Important to note that the both aromaticity indexes that are based on geometrical and electronic characteristics predict a similar behavior of the systems. Thus, the higher stability of the CT2 state, where the fullerene acts as the electron donor, is caused at least in part by the gain in aromaticity and stability of **[4]PP**, which acts as an electron acceptor.

Effects of environment

The COSMO-like model[59] with dichloromethane (DCM) as a solvent was applied to estimate the effect of polar environment on electronic excitations. Application of this model previously showed a good agreement of computational results with experimental data for excited state energies of $Li^{+}@C_{60}\subset$[10]CPP and ZnP–[10]CPP$\supset C_{60}$ complexes.[60-63] The dipole moment of the studied **[4]DHPP$\supset$C$_{60}$** and **[4]PP$\supset$C$_{60}$** complexes was found to be 0.28 and 0.22 D, respectively. Their small values can be explained by high symmetry of the fragments and high ability of fullerene and nanohoops to delocalize the charge excess. The ground state (GS) solvation energies for **[4]DHPP$\supset$C$_{60}$** and **[4]PP$\supset$C$_{60}$** are equal to -0.89 and -0.62 eV, respectively. A change in the dipole moment ($\Delta\mu$) due to GS $\rightarrow$ LE excitations is rather small and does not exceed 0.40 D. Thus, the solvation energies of the LE^{Host} and LE^{Guest} states are very similar to those in the GS. Usually the solvation energies of CT states are significantly higher due to polarity of systems. However, it is known that for fullerene complexes with symmetric CPPs and their π-extended analogs the solvation energy of CT states does not differ much from the energy of GS.[64,65] The obtained results show that the difference in dipole moments between CT1 and GS states in **[4]DHPP$\supset$C$_{60}$** does not exceed 2 D. Consequently, the solvation energy of the CT1 state is -0.91 eV. Detailed solvation data in DCM are given in Table S7, SI. Important to note that for **[4]DHPP$\supset$C$_{60}$** the CT1 state is the lowest excited state even in the gas phase. Figure 4 displays the energies of LE and CT states as well as simulated absorption spectra for the complexes.

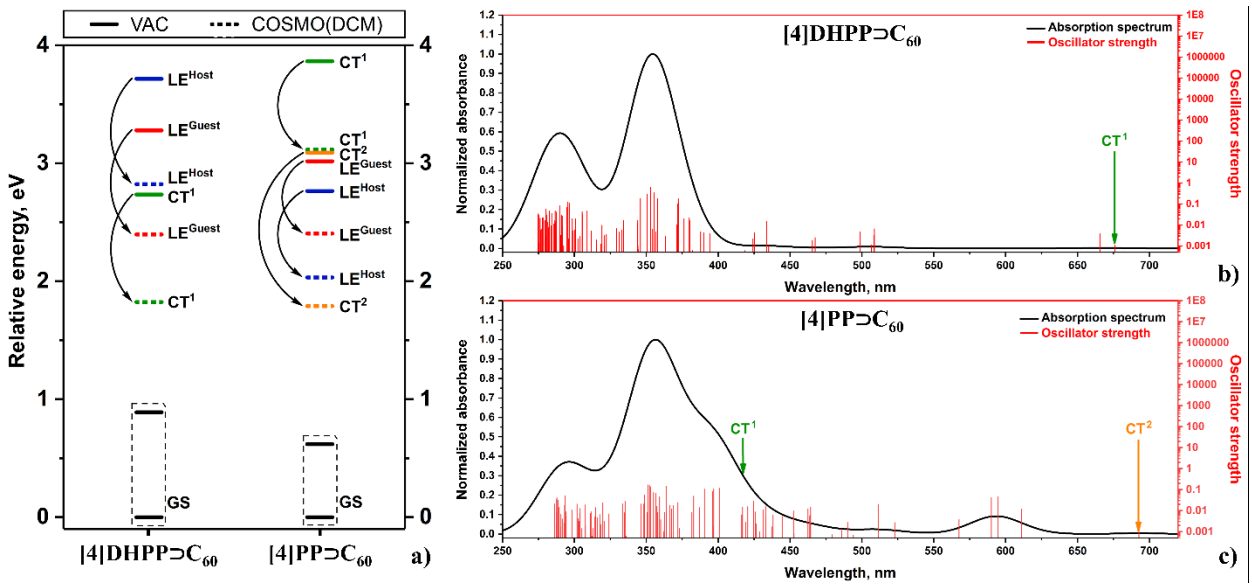

Figure 4. (a) Energies of LE and CT states in **[4]DHPP⊃C$_{60}$** and **[4]PP⊃C$_{60}$** in vacuum (VAC) and dichloromethane (DCM). Simulated spectra of **[4]DHPP⊃C$_{60}$** (b) and **[4]PP⊃C$_{60}$** (c) in DCM. The absorption spectra were constructed using Gaussian broadening (FWHM=0.20 eV). The red vertical lines show the oscillator strength for 120 lowest singlet excited states.

For **[4]PP⊃C$_{60}$**, $\Delta\mu$ for GS $\rightarrow$ CT1 transition and solvation energies are 4.24 D and -0.75 eV, whereas for the CT2 state these values are 7.63 D and -1.30 eV, respectively. The charge transfer values in both cases are almost the same (0.912 and 0.905 ***e*** for CT1 and CT2) and thus cannot explain the observed difference in the solvation. Analysis of NTOs describing the CT1 and CT2 processes indicates that the orbital on nanohoop fragment is more localized in the CT2 state than in the CT1 state, where the charge is delocalized over the host. The inverse participation ratio (IPR) that counts the number of atoms involved in the charge delocalization was used to quantify the observed difference.[64] The IPR for **[4]PP** in the CT1 and CT2 states equal to 35 and 31 (Table S8, SI). The IPR values for **C$_{60}$** show the same trend: 25 in CT2 *vs* 33 in CT1. Thus, the difference in solvation energies of the CT states well correlates with the difference in the IPR for the host and guest fragments. The same conclusion can be drawn based on molecular electrostatic potential (MEP). A comparison of the MEPs for CT1 and CT2 demonstrates a qualitative difference between these states (Figure 5). In the CT1 state, the **[4]PP** nanohoop is positively charged. However at MEP clearly seen negatively charged spots around the nitrogen atoms and positively charged areas over carbon atoms. In the case of the CT2 state, the nanohoop is charged negatively, and MEP is fairly evenly distributed over the ring. As expected, the close proximity of positive and negative spots on MEP in the case of CT1 reduces its solvation energy compared to the CT2 state.

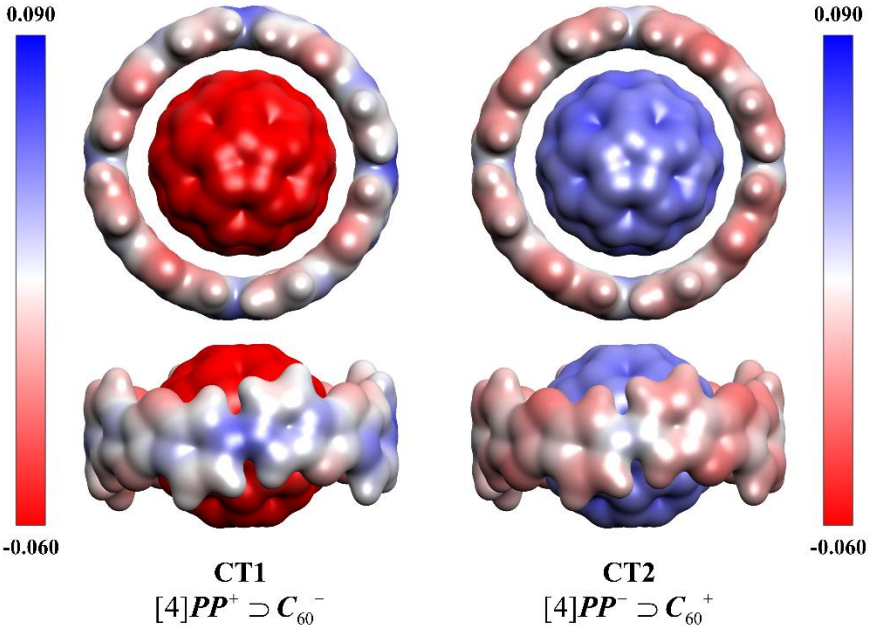

Figure 5. Molecular electrostatic potential surfaces calculated for CT1 and CT2 states of the **[4]PP⊃C$_{60}$** complex. The surfaces are drawn at electron density contours of 0.03 e/Å^3 and colored according to the value of the electrostatic potential.

Summing up, the stabilization of the CT2 state in **[4]PP⊃C$_{60}$** complex by polar solvent is sufficient to rearrange this state with the LE states when passing from the gas phase to DCM and to make CT2 the lowest excited state. However, the stabilization of CT1 is relatively small and this state remains higher in energy than the LE states.

Electron transfer rates

The CT states of the complexes are characterized by a very weak oscillator strength and therefore cannot be directly populated by light absorption. A decay of both types of LE state (LE^{Guest} and LE^{Host}) was considered as the main process of formation of the CT states. Exciton transfer ($LE^{Host} \rightarrow LE^{Guest}$) or intersystem crossing ($LE^{S} \rightarrow LE^{T}$) processes are much slower and do not compete with the generation of the CT state (Table S9). The rates of electron transfer (k_{ET}) and charge recombination (k_{CR}) processes were calculated using the semi-classical method by Ulstrup and Jortner.[66] This method has proven to be reliable for the covalent all-fullerene C_{60}-$Lu_3N@I_h$-C_{80} and non-covalent complex of doubly curved nanographene with C_{60} fullerene.[8,58] Within this approach, the intramolecular relaxation associated with ET is described by an effective vibrational mode, and the rate is controlled by four parameters: electronic coupling of the initial and final states V_{ij}, solvation reorganization energy λ_s, reaction Gibbs energy ΔG^0, and effective Huang-Rhys factor S_{eff}. The rates were estimated using the effective frequency of 1600 cm^{-1}, which corresponds to the stretching of C=C bonds. Previously we showed that the charge separation rate in nanoring-fullerene complexes does not change significantly by varying the effective frequency from 1400 to 1800 cm^{-1}.[60,64] The calculated k_{ET} and k_{CR} rates in DCM are listed in Table 4.

Table 4. Gibbs energy ΔG^0 (in eV), electronic coupling $|V_{ij}|$ (in eV), reorganization energy λ (in eV), Huang-Rhys factor (S_{eff}), activation energy E_a (in eV), and rates k_X (in s^{-1}) for ET and CR processes in **[4]DHPP⊃C$_{60}$** and **[4]PP⊃C$_{60}$** complexes computed in DCM.

Complex XXX⊃C$_{60}$	Transition	$\Delta G^{0[a]}$	$\|V_{ij}\|$	λ	S_{eff}[b]	E_a	k_X
[4]DHPP	$LE^{Guest} \rightarrow CT1$	-0.573	$1.96\cdot10^{-3}$	0.376	0.998	0.012	$3.60\cdot10^{10}$
	$LE^{Host} \rightarrow CT1$	-1.000	$6.58\cdot10^{-3}$	0.367	0.998	0.015	$3.05\cdot10^{10}$
	$CT1 \rightarrow GS$	-1.824	$2.38\cdot10^{-2}$	0.311	0.746	0.024	$2.35\cdot10^{7}$
[4]PP	$LE^{Guest} \rightarrow CT1$	0.712	$6.21\cdot10^{-2}$	0.356	1.185	1.432	$[1.09\cdot10^{-10}]$
	$LE^{Host} \rightarrow CT1$	1.114	$4.43\cdot10^{-3}$	0.354	1.185	3.191	$[1.09\cdot10^{-43}]$
	$CT1 \rightarrow GS$	n/a					
	$LE^{Guest} \rightarrow CT2$	-0.615	$1.34\cdot10^{-2}$	0.309	0.781	0.013	$9.53\cdot10^{11}$
	$LE^{Host} \rightarrow CT2$	-0.243	$1.71\cdot10^{-2}$	0.307	0.781	0.015	$9.58\cdot10^{12}$
	$CT2 \rightarrow GS$	-1.790	$1.73\cdot10^{-2}$	0.284	0.711	0.021	$9.75\cdot10^{6}$

[a] Gibbs energy difference between the given states. [b] Effective value of the Huang-Rhys factor $S_{eff} = \lambda_I / \hbar\omega_{eff}$, where $\hbar\omega_{eff}$ is set to 1600 cm^{-1}

As seen, the charge separation in **[4]DHPP⊃C$_{60}$** is characterized by a significant negative Gibbs energy. The decay of both LE states to the CT1 takes place in the inverted Marcus region ($|\Delta G^0| > \lambda$). The rate of the CT1 generation from LE^{Guest} and LE^{Host} was found to be $3.60\cdot10^{10}$ and $3.05\cdot10^{10}$ s^{-1}, respectively. In turn, the charge recombination reaction ($CT1 \rightarrow GS$) occurs in a deep inverted Marcus region ($|\Delta G^0| \gg \lambda$, Figure S12), and its rate is three orders of magnitude slower than the CS rates. In the case of **[4]PP⊃C$_{60}$** complex with antiaromatic fragments, there are two possible CT states. Generation of the CT1 state, where electron is transferred from **[4]PP** to **C$_{60}$**, from both LE^{Guest} and LE^{Host} is very unlikely because of its highly positive Gibbs energy and extremely high activation energy. However, the formation of the CT2 state, where fullerene acts as electron donor, is characterized by rather small activation energies and occurs on picosecond timescale. In particular, characteristic time were found to be 1.1 and 0.1 ps for $LE^{Guest} \rightarrow CT2$ and $LE^{Host} \rightarrow CT2$, correspondingly. A good addition to this is a relatively slow charge recombination $CT2 \rightarrow GS$ reaction (Table 4), which suggest a quite long CT state lifetime. There are only a few reports, in which fullerene has been used as an electron donor in combination with strong electron acceptors. Among them, the complexes with trinitrofluorenone,[67] subphthalocyanines,[68] and xanthylium[69] shows intramolecular PET, whereas complexes with p-chloranil[70] and [10]-perfluorocycloparaphenylene[65] are the rare examples of intermolecular PET from fullerene to strong electron acceptor.

Conclusions

In this work, using DFT/TD-DFT approach, we studied the ground and excited state properties of the **[4]DHPP** and **[4]PP** nanohoops containing the aromatic and antiaromatic fragments, respectively. Antiaromatic **[4]PP** exhibits significantly lower energies of HOMO and LUMO compared to **[4]DHPP**, which improves electron-accepting but disfavors electron-donating properties of the nanohoop. The PET properties of the host-guest complexes with **C$_{60}$** are determined by the electronic nature of nanohoops. The ET from nanohoop to **C$_{60}$** in **[4]DHPP⊃C$_{60}$** occurs in the inverted Marcus region on the nanosecond timescale. In contrast, the population of such CT state in **[4]PP⊃C$_{60}$** does not seem feasible. However, the ET from **C$_{60}$** to **[4]PP** is almost barrierless and characterized by ultrafast PET occurring on the picosecond timescale. To the best of our knowledge, **[4]PP⊃C$_{60}$** complex is a rare example of non-covalent complexes

showing photooxidation of fullerene. We believe that the predictions made in this work will arouse additional interest among synthetic organic chemists in new and so far little studied nanorings containing antiaromatic fragments.

Conflicts of interest

There are no conflicts to declare.

Author contributions

G.G. Investigation, Formal analysis, Writing – original draft, Writing – review & editing
O. A. S. Investigation, Formal analysis, Writing – original draft, Writing – review & editing
A. A. V. Supervision, Writing – review & editing
A. J. S. Investigation, Supervision, Writing – review & editing
M. S. Supervision, Writing – review & editing, Funding acquisition

Acknowledgements

We are grateful for financial support from the Spanish Ministerio de Ciencia e Innovación (Network RED2018-102815-T, project PID2020-113711GB-I00, and Juan de la Cierva contract IJC2019-039846-I to A.J.S.), the Catalan Conselleria de Recerca i Universitats of the Generalitat de Catalunya (project 2017SGR39 and contract 2020 FISDU 00345 to G.G.) and the University of Girona (POSTDOC-UdG 2021/31 to O.A.S.). This research was supported in part by PLGrid Infrastructure.

References

1. Y. Segawa, H. Ito and K. Itami, *Nat. Rev. Mater.*, 2016, **1**, 15002.
2. Y. Segawa, D. R. Levine and K. Itami, *Acc. Chem. Res.*, 2019, **52**, 2760-2767.
3. D. Wu, W. Cheng, X. Ban and J. Xia, *Asian J. Org. Chem.*, 2018, **7**, 2161-2181.
4. E. J. Leonhardt and R. Jasti, *Nat. Rev. Chem.*, 2019, **3**, 672-686.
5. K. Yazaki, L. Catti and M. Yoshizawa, *Chem. Commun.*, 2018, **54**, 3195-3206.
6. D. Lu, Q. Huang, S. Wang, J. Wang, P. Huang and P. Du, *Front. Chem.*, 2019, **7**.
7. Y. Xu and M. von Delius, *Angew. Chem. Int. Ed.*, 2020, **59**, 559-573.
8. S. Zank, J. M. Fernández-García, A. J. Stasyuk, A. A. Voityuk, M. Krug, M. Solà, D. M. Guldi and N. Martín, *Angew. Chem. Int. Ed.*, 2022, **61**, e202112834.
9. B. Esser and M. Hermann, *Nat. Chem.*, 2021, **13**, 209-211.
10. M. Hermann, D. Wassy and B. Esser *Angew. Chem. Int. Ed.*, 2021, **60**, 15743-15766.
11. S. E. Lewis, *Chem. Soc. Rev.*, 2015, **44**, 2221-2304.
12. Y. Segawa, A. Yagi, K. Matsui and K. Itami, *Angew. Chem. Int. Ed.*, 2016, **55**, 5136-5158.
13. H. Omachi, Y. Segawa and K. Itami, *Acc. Chem. Res.*, 2012, **45**, 1378-1389.
14. E. R. Darzi and R. Jasti, *Chem. Soc. Rev.*, 2015, **44**, 6401-6410.
15. M. Fujitsuka, D. W. Cho, T. Iwamoto, S. Yamago and T. Majima, *Phys. Chem. Chem. Phys.*, 2012, **14**, 14585-14588.
16. A. Minsky, A. Y. Meyer and M. Rabinovitz, *Tetrahedron*, 1985, **41**, 785-791.
17. N. S. Mills, A. Levy and B. F. Plummer, *J. Org. Chem.*, 2004, **69**, 6623-6633.
18. J. Cao, G. London, O. Dumele, M. von Wantoch Rekowski, N. Trapp, L. Ruhlmann, C. Boudon, A. Stanger and F. Diederich, *J. Am. Chem. Soc.*, 2015, **137**, 7178-7188.
19. M. Rosenberg, C. Dahlstrand, K. Kilså and H. Ottosson, *Chem. Rev.*, 2014, **114**, 5379-5425.

20. P. B. Karadakov, *J. Phys. Chem. A*, 2008, **112**, 7303-7309.
21. R. Papadakis and H. Ottosson, *Chem. Soc. Rev.*, 2015, **44**, 6472-6493.
22. D. Wassy, M. Pfeifer and B. Esser, *J. Org. Chem.*, 2020, **85**, 34-43.
23. J. S. Wössner, D. Wassy, A. Weber, M. Bovenkerk, M. Hermann, M. Schmidt and B. Esser, *J. Am. Chem. Soc.*, 2021, **143**, 12244-12252.
24. M. Hermann, D. Wassy, J. Kohn, P. Seitz, M. U. Betschart, S. Grimme and B. Esser, *Angew. Chem. Int. Ed.*, 2021, **60**, 10680-10689.
25. J. S. Wössner, J. Kohn, D. Wassy, M. Hermann, S. Grimme and B. Esser, *Org. Lett.*, 2022, **24**, 983-988.
26. O. A. Stasyuk, A. J. Stasyuk, M. Solà and A. A. Voityuk, *Nanoscale Adv.*, 2022, **4**, 2180-2188.
27. A. J. Stasyuk, O. A. Stasyuk, M. Solà and A. A. Voityuk, *Dalton Trans.*, 2021, **50**, 16214-16222.
28. O. Stephan, P. M. Ajayan, C. Colliex, P. Redlich, J. M. Lambert, P. Bernier and P. Lefin, *Science*, 1994, **266**, 1683-1685.
29. J. Usuba and A. Fukazawa, *Chem. Eur. J.*, 2021, **27**, 16127-16134.
30. A. Iida, A. Sekioka and S. Yamaguchi, *Chem. Sci.*, 2012, **3**, 1461-1466.
31. L. Qiu, C. Yu, N. Zhao, W. Chen, Y. Guo, X. Wan, R. Yanga and Y. Liu, *Chem. Commun.*, 2012, **48**, 12225-12227.
32. L. Qiu, X. Zhuang, N. Zhao, X. Wang, Z. An, Z. Lan and X. Wan, *Chem. Commun.*, 2014, **50**, 3324-3327.
33. A. D. Becke, *Phys. Rev. A*, 1988, **38**, 3098-3100.
34. C. Lee, W. Yang and R. G. Parr, *Phys. Rev. B*, 1988, **37**, 785-789.
35. F. Weigend and R. Ahlrichs, *Phys. Chem. Chem. Phys.*, 2005, **7**, 3297-3305.
36. F. Weigend *Phys. Chem. Chem. Phys.*, 2006, **8**, 1057-1065.
37. B. Brauer, M. K. Kesharwani, S. Kozuch and J. M. L. Martin, *Phys. Chem. Chem. Phys.*, 2016, **18**, 20905-20925.
38. R. Sedlak, T. Janowski, M. Pitoňák, J. Řezáč, P. Pulay and P. Hobza, *J. Chem. Theory Comput.*, 2013, **9**, 3364-3374.
39. T. Yanai, D. P. Tew and N. C. Handy, *Chem. Phys. Lett.*, 2004, **393**, 51-57.
40. P. Besalú-Sala, A. A. Voityuk, J. M. Luis and M. Solà, *Phys. Chem. Chem. Phys.*, 2021, **23**, 5376-5384.
41. J. Kruszewski and T. M. Krygowski, *Tetrahedron Lett.*, 1972, **13**, 3839-3842.
42. T. M. Krygowski, *J. Chem. Inf. Model.*, 1993, **33**, 70-78.
43. D. W. Szczepanik, M. Andrzejak, K. Dyduch, E. Żak, M. Makowski, G. Mazur and J. Mrozek, *Phys. Chem. Chem. Phys.*, 2014, **16**, 20514-20523.
44. D. W. Szczepanik, M. Andrzejak, J. Dominikowska, B. Pawełek, T. M. Krygowski, H. Szatylowicz and M. Solà, *Phys. Chem. Chem. Phys.*, 2017, **19**, 28970-28981.
45. P. v. R. Schleyer, C. Maerker, A. Dransfeld, H. Jiao and N. J. R. van Eikema Hommes, *J. Am. Chem. Soc.*, 1996, **118**, 6317-6318.
46. Z. Chen, C. S. Wannere, C. Corminboeuf, R. Puchta and P. v. R. Schleyer, *Chem. Rev.*, 2005, **105**, 3842-3888.
47. D. Geuenich, K. Hess, F. Köhler and R. Herges, *Chem. Rev.*, 2005, **105**, 3758-3772.
48. G. J. Bodwell, J. N. Bridson, M. K. Cyrañski, J. W. J. Kennedy, T. M. Krygowski, M. R. Mannion and D. O. Miller, *J. Org. Chem.*, 2003, **68**, 2089-2098.
49. G. J. Bodwell, J. N. Bridson, T. J. Houghton, J. W. J. Kennedy and M. R. Mannion, *Chem. Eur. J.*, 1999, **5**, 1823-1827.
50. F. Feixas, E. Matito, J. Poater and M. Solà, *J. Phys. Chem. A*, 2007, **111**, 4513-4521.
51. K. Morokuma, *Acc. Chem. Res.*, 1977, **10**, 294-300.
52. T. Ziegler and A. Rauk, *Theor. Chim. Acta*, 1977, **46**, 1-10.

53. ADF 2017, S., Theoretical Chemistry, Vrije Universiteit, Amsterdam, The Netherlands, http://www.scm.com. ADF 2017, SCM, Theoretical Chemistry, Vrije Universiteit, Amsterdam, The Netherlands, http://www.scm.com.
54. R. F. W. Bader, *Chem. Rev.*, 1991, **91**, 893-928.
55. E. R. Johnson, S. Keinan, P. Mori-Sánchez, J. Contreras-García, A. J. Cohen and W. Yang, *J. Am. Chem. Soc.*, 2010, **132**, 6498-6506.
56. K. Yuan, C.-H. Zhou, Y.-C. Zhub and X. Zhao, Phys. Chem. Chem. Phys., 2015, **17**, 18802-18812.
57. I. González-Veloso, J. Rodríguez-Otero and E. M. Cabaleiro-Lago, Phys. Chem. Chem. Phys., 2016, **18**, 31670-31679.
58. M. Izquierdo, B. Platzer, A. J. Stasyuk, O. A. Stasyuk, A. A. Voityuk, S. Cuesta, M. Sola, D. M. Guldi and N. Martin, *Angew. Chem. Int. Ed.*, 2019, **58**, 6932-6937.
59. A. Klamt, *J. Phys. Chem.*, 1996, **100**, 3349-3353.
60. A. J. Stasyuk, O. A. Stasyuk, M. Solà and A. A. Voityuk, *J. Phys. Chem. B*, 2020, **124**, 9095-9102.
61. A. J. Stasyuk, O. A. Stasyuk, M. Solà and A. A. Voityuk, *Chem. Commun.*, 2019, **55**, 11195-11198.
62. H. Ueno, T. Nishihara, Y. Segawa and K. Itami, *Angew. Chem., Int. Ed.*, 2015, **54**, 3707-3711
63. Y. Xu, B. Wang, R. Kaur, M.B. Minameyer, M. Bothe, T. Drewello, D. M. Guldi and M. A. von Delius, *Angew. Chem., Int. Ed.*, 2018, **57**, 11549-11553.
64. A. J. Stasyuk, O. A. Stasyuk, M. Solà and A. A. Voityuk, *Chem. Commun.*, 2020, **56**, 12624-12627.
65. O. A. Stasyuk, A. J. Stasyuk, M. Solà and A. A. Voityuk, *ChemPhysChem*, **n/a**, e202200226.
66. J. Ulstrup and J. Jortner, *J. Chem. Phys.*, 1975, **63**, 4358-4368.
67. K. Ohkubo, J. Ortiz, L. Martín-Gomis, F. Fernández-Lázaro, Á. Sastre-Santos and S. Fukuzumi, Chem. Commun., 2007, 589-591.
68. M. Rudolf, O. Trukhina, J. Perles, L. Feng, T. Akasaka, T. Torres and D. M. Guldi, Chem. Sci., 2015, **6**, 4141-4147.
69. H. Kano, K. Matsuo, H. Hayashi, K. Kato, A. Yamakata, H. Yamada and N. Aratani, Eur. J. Org. Chem. 2021, 3377-3381.
70. S. Fukuzumi, H. Mori, H. Imahori, T. Suenobu, Y. Araki, O. Ito and K. M. Kadish, J. Am. Chem. Soc., 2001, **123**, 12458–12465.